1 **Impact of Heating Anomalies Associated with Rainfall Variations over the**

2 **Indo-Western Pacific on Asian Atmospheric Circulation in Winter**

3

4 Jian Zheng [1*]

5 Qinyu Liu [1]

6 Chunzai Wang [2]

7 Xiao-Tong Zheng [1]

8

9 [1] Physical Oceanography Lab., Key Lab. of Ocean-Atmosphere Interaction and

10 Climate in Universities of Shandong, Ocean University of China, Qingdao, 266100,

11 China

12 [2] Physical Oceanography Division, NOAA Atlantic Oceanographic and

13 Meteorological Laboratory, Miami, Florida, 33149, USA

14

17 *Corresponding author

18 Jian Zheng

19 College of Physical and Environmental Oceanography, Ocean University of China,

20 Qingdao, 266100, China.

21 Phone: +1-303-492-8653(o)

22 E-mail: jian.zheng@colorado.edu

23

Abstract

Observational data show that the dominant mode of the boreal winter rainfall anomalies in the tropical Indo-Western Pacific (IWP) is a west-east dipolar pattern, which is called the Indo-Western Pacific Dipole (IWPD) mode and is related to ENSO. It is found that corresponded to the IWPD mode is a new atmospheric teleconnection pattern – a wave train pattern emitted from the IWP toward Asia and the northwest Pacific in winter. During the positive (negative) phase of the IWPD, the teleconnection pattern features the negative (positive) anomalies of 200-hPa geopotential height (H200) centered at 30°N, 110°E and the positive (negative) anomalies of H200 centered at 45°N, 140°E. The teleconnection pattern represents the dominant mode of the boreal winter H200 anomaly over Asia. A series of simple atmospheric model experiments are performed to confirm that this winter teleconnection pattern is induced by the heating anomalies associated with the IWPD, and the heating anomalies over the equatorial central Pacific are not important to this teleconnection pattern from the IWP toward Asia and the northeast Pacific. The IWPD is strengthened after the climate regime shift of the 1970s, which leads to a stronger teleconnection pattern.

Key words: tropical Indo-Western Pacific; rainfall; teleconnection; East Asia; decadal change

1. Introduction

El Niño-Southern Oscillation (ENSO) is a dominant mode of climate variability in Earth's climate system. ENSO has profound influences not only on the tropics but also on the midlatitude (e.g., Kelin et al. 1999; Alexander et al. 2002). The diabatic heating anomaly over the central equatorial Pacific during ENSO can excite a stationary barotropic Rossby wave train propagating into extratropical regions. This teleconnection is known as the Pacific-North American (PNA) pattern (Wallace and Gutzler 1981) in the Northern Hemisphere and the Pacific-South American (PSA) pattern (Robertson and Mechoso 2003) in the Southern Hemisphere. For El Niño, the PNA-like pattern is usually characterized as negative height anomalies over the North Pacific, positive anomalies over western Canada, and negative anomalies over the southeastern United States (Horel and Wallace 1981). The theoretical work of Hoskins and Karoly (1981) indicates a ray path connecting the anomaly centers of the PNA wave train, which is directed first poleward, then curved eastward, and finally directed back equatorward.

Zhang et al. (1996) pointed out that when El Niño matures in boreal winter, the anomalous circulation is characterized by an anomalous subsidence over the maritime continent, an anomalous anticyclone over the tropical western North Pacific (Wang et al. 1999), and a reversed Hadley circulation in the western Pacific. The atmospheric circulation in the Pacific during the different phases of ENSO is shown in Wang (2002). The convective activity and atmospheric circulation in the western Pacific are related to ENSO events in the tropical eastern Pacific.

69   The teleconnection between the tropics and extratropics also occurs over the

70   tropical western Pacific and Asia. Nitta (1987) found an association between

71   abnormal convective activity over the tropical western North Pacific and atmospheric

72   circulation anomalies over the midlatitude of East Asia in summer (June to August;

73   JJA). This teleconnection was named as the Pacific-Japan (PJ) pattern. Associated

74   with the PJ pattern are a gain of kinetic energy and available potential energy through

75   barotropic and baroclinic energy conversions from the climatological mean state

76   (Kosaka and Nakamura 2010), in addition to available potential energy supplied by

77   anomalous diabatic heating in the tropical western North Pacific. The impact of the

78   tropical western Pacific on the East Asian summer monsoon is also studied by Huang

79   and Sun (1992). They pointed out that the summer monsoon rainfall might be weak in

80   the Yangtze River and the Huaihe River valley, when the convective activity around

81   the Philippines is intensified.

82   These previous studies mainly focused on the remote influence of heating anomaly

83   over the tropical western Pacific on Asian summer climate. What is the influence of

84   the heating anomaly in the tropical Indo-Western Pacific (IWP) during winter? Can

85   the heating anomalies associated with rainfall variations in the IWP affect the winter

86   climate in East Asia? The rainfall anomalies are observed to show two large

87   variations centered in the central equatorial Pacific and in the tropical IWP (Fig. 1) in

88   boreal winter (December to February; DJF). The large rainfall anomalies over the

89   central equatorial Pacific are accompanied with the PNA-like pattern and have been

90   extensively studied previously. The present paper emphasizes the second large rainfall

91   variation over the IWP, with its rainfall variability in winter comparable with that in

92   summer (Fig. 1). The purpose of this paper is to investigate whether and how the

93   winter rainfall variability over the IWP can trigger atmospheric teleconnection to the

94   midlatitudes of Asia and the northwest Pacific. Furthermore, Indo-Pacific climate

95   displays noticeable changes across the 1976/77 climate regime shift (e.g., Trenberth

96   and Hurrel 1994), and the influence of the tropical Indian Ocean on the western

97   Pacific and East Asian climate is intensified after the late 1970s (Xie et al. 2010). It is

98   still unknown whether similar decadal change exists in the IWP rainfall variability

99   and its teleconnected influence.

100   The rest of the paper is organized as follows. Section 2 describes the data and

101   model used in this study. Sections 3 and 4 present the leading mode of rainfall

102   variability over the IWP and its impact on Asia and the northwest Pacific based on

103   observational analysis and model experiments. Section 5 provides a summary and

104   discussion.

105

106   **2. Data and model**

107   *2.1. Data*

108   Two sets of rainfall data are used in this study. One is from the Climate Prediction

109   Center (CPC) Merged Analysis of Precipitation (CMAP) (Xie and Arkin 1997) from

110   1979 to 2008. The other one is NOAA's Precipitation Reconstruction Dataset (PREC)

111   (Chen et al. 2002; Akin and Smith 2003), available on a 2.5° grid for 1948-2009. The

112   climatology is based on the time periods of 1951-1990 over land and 1979-1998 over

oceans. The other atmospheric data set is from the National Centers for Environmental Prediction/National Center for Atmospheric Research (NCEP/NCAR) reanalysis (Kalnay et al. 1996). SST data set is from the monthly National Oceanic and Atmospheric Administration Extended Reconstructed Sea Surface Temperature V3b (NOAA ERSST V3b) (Smith et al. 2008).

First, we examine the rainfall interannual variability for the period of 1979-2008 based on the CMAP data. Then the interdecadal modulations in the interannual variability before and after the 1976/77 climate shift are examined by using the PREC data. To focus on interannual variations, the detrending and 7-yr high pass filtering are performed to monthly anomalies in this study.

2.2. Atmospheric model

A simple atmospheric model, which is developed by Lee et al. (2009), is used to gain insight into the atmospheric response to heating forcing over the IWP. The model is a steady-state two-level (centered at 250 hPa and 750 hPa) spherical-coordinate primitive equation model, linearized about a specified background flow. The model uses triangular 18 truncations for horizontal grid. The atmospheric mean flow states are climatological mean for boreal winter and vary zonally for the experiments in this study. The detailed description of the simple model is given by Lee et al. (2009).

Some model results of both the local and remote responses of the atmosphere to tropical heating anomalies over the equatorial central Pacific are demonstrated by Lee et al. (2009). Besides, the model successfully simulated the interhemispheric

135 connection between the Atlantic warm pool and the southeastern tropical Pacific

136 (Wang et al. 2010).

137

138 **3. Leading mode of rainfall variability over the IWP**

139 In order to obtain the spatio-temporal rainfall variability over the IWP in winter, we

140 perform an empirical orthogonal function (EOF) analysis of CMAP winter rainfall

141 anomalies in the domain of 20°S-20°N, 40-160°E. As shown in Fig. 2, the first EOF

142 mode (EOF1) explains about 36.9% of the total variance for the period of 1979-2008.

143 For the positive (negative) phase of EOF1, the spatial patterns show a west-east

144 dipolar pattern with more (less) rainfall over the tropical western Indian Ocean (WIO)

145 and less (more) over the tropical eastern Indian Ocean-western Pacific (EI-WP) (Fig.

146 2a). Over the tropical Indian Ocean, the spatial pattern is similar to the rainfall

147 anomaly pattern for the Indian Ocean Dipole (IOD) mode (Saji et al. 1999). Hereafter,

148 the EOF1 is called the Indo-Western Pacific Dipole (IWPD) mode, and the positive

149 phase of the IWPD is defined as more (less) rainfall over the WIO (EI-WP). As

150 shown in the PC1 time series, the extreme events of the IWPD usually appear in

151 ENSO years, such as 1982 and 1997 (Fig. 2b). The simultaneous correlation between

152 PC1 and the Niño3.4 index is 0.87 (exceeding the 99% confidence level). The IWPD

153 is also correlated with the IOD. The correlation between PC1 and the IOD index in

154 prior months of September-November is 0.68, which is statistically significant at the

155 99% level. It is noted that 1982 and 1997 are also IOD years. An extreme IOD event

156 also appears in fall of 1994 (Saji et al. 1999), but there is no significant rainfall

variation associated with the IWPD in the winter of 1994 (Fig. 2b). The partial

correlation between PC1 and the IOD index by removing the Nino3.4 influence is

0.49, and the partial correlation between PC1 and Nino3.4 by removing the IOD

influence is 0.70. Thus, the IWPD is closely related to the IOD events which occur

concomitantly with ENSO.

The spatial patterns of EOF2 show more rainfall over the southern tropical Indian

Ocean and less rainfall north of Australia and east to New Guinea (not shown). EOF2

accounts for only 11% of the total variance. In this study, we therefore focus only on

the teleconnected impact of the IWPD on Asian atmospheric circulation.

4. Influence of IWPD on Asia and the Northwest Pacific

4.1. Observational results

We use the linear regression analysis to examine the possible impact of the IWPD

on Asian and northwest Pacific climate in winter. Figure 3 shows the regression maps

of oceanic and atmospheric variables onto PC1 time series. The SST anomalies show

an El Niño-like pattern in the tropical Pacific, indicating that the IWPD is related to

ENSO (Fig. 3a). The tropical SST anomalies appear as a zonal tripole, with warm

anomalies in the tropical Indian Ocean and eastern equatorial Pacific and cold

anomalies in the Maritime Continent/tropical western Pacific.

For the anomalies of 200-hPa geopotential height (H200), there are two

anticyclones straddled in the equatorial eastern Pacific associated with the positive

phase of the IWPD. These anomalous anticyclones are the reminiscent pair of Rossby

179　wave in Matsuno-Gill type of response to the heating anomaly over the equatorial

180　central Pacific (Matsuno 1966; Gill 1980). Over the IWP, the H200 anomaly shows a

181　wedge-shape, which is associated with Kelvin wave produced by the rainfall anomaly

182　in the tropical Indian Ocean. In extratropical regions, the H200 anomaly shows two

183　wave trains (Fig. 3a). One is the PNA-like pattern, which is induced by the heating

184　associated with the warm SST anomalies in the equatorial eastern Pacific. The other

185　wave train is emitted from the IWP toward Asia and the northwest Pacific, with

186　reduced H200 over Asia (centered in 30°N, 110°E) and enhanced H200 over the

187　northeast part of China/Korean Peninsula/Japan (centered at 45°N, 140°E) during the

188　IWPD positive phase. At lower level, the circulation anomalies associated with the

189　IWPD show low sea level pressure (SLP) anomalies over midlatitude/subpolar Asia

190　and high SLP anomalies over Japan and South Asia. Besides, consistent with the SST

191　anomalies, easterly surface wind anomalies appear over the equatorial Indian Ocean

192　and the far western equatorial Pacific (Wang et al. 1999), and westerly anomalies over

193　the equatorial central Pacific. These indicate that the Walker circulation weakens both

194　in the tropical Indian Ocean and in the tropical Pacific in association with the positive

195　phase of the IWPD.

196　　The relationships of the IWPD with SST and surface wind in the season of

197　September-November (SON) are shown by the regression map of SON SST and sea

198　surface wind onto PC1 time series (Fig. 3c). The SST pattern is IOD-like in the

199　tropical Indian Ocean and El Niño-like in the tropical Pacific. According to previous

200　studies, the feedback effect of SST to atmosphere can be derived by regression of the

atmospheric anomalies upon the leading SST anomalies (Frankignoul et al., 1998; Liu et al., 2006; Fan et al. 2010). Thus, the DJF rainfall dipolar pattern over the IWP could be the union response to the SST anomalies in the tropical Indian Ocean and tropical Pacific during SON (Fig. 3c). The positive SST anomaly over the tropical Indian Ocean east to 80°E in DJF (Fig. 3a) could be result of local reduced cloud cover and wind anomaly as responses to the El Niño (Klein et al. 1999; Reason et al. 2000; Yang et al. 2007). However, we should keep in mind that large rainfall anomalies do not necessarily follow high SST anomalies, similar to the rainfall-SST distribution in the tropical Pacific during El Niño (the positive rainfall anomalies are located in the equatorial central Pacific, but high SST anomalies are normally resided in the equatorial eastern Pacific). During SON, associated with the SST anomalies are easterly wind anomalies in the equatorial Indian Ocean and westerly wind anomalies in the equatorial central and eastern Pacific. As in the case during winter, these variations indicate that the Walker circulation weakens both in the tropical Indian Ocean and in the tropical Pacific. Previous studies have shown El Niño could reduce the rainfall and suppress the convection over the western Pacific through the change of the Walker circulation (e.g., Zhang et al. 1996; Wang 2002; Alexander et al. 2004). Yang et al. (2010) also showed the dipolar rainfall pattern over the IWP during November-January is related to the preceding IOD-like SST anomalies during October-December (their Fig.8). Thus, the developing El Niño in SON and the matured IOD will lead to the IWPD mode, which emits the wave train from the IWP to East Asia and the northwest Pacific in the following winter.

223   To determine whether the wave train is the primary mode of interannual variability

224   of atmospheric circulation, an EOF analysis is performed using the H200 anomaly in

225   the domain of 20°S-70°N, 0°-180° during winter (DJF). The spatial pattern and time

226   series of the first mode are shown in Fig. 4. EOF1 accounts for 23.3% of the total

227   variance for the period of 1979-2008. The spatial structure of EOF1 features

228   below-normal height over East China and above-normal height extending from

229   Balkhash to the northwestern Pacific. The pattern resembles the wave train in the

230   regression map. The PC1 time series shows that the extreme events of EOF1 often

231   occur in ENSO years, being similar to the IWPD. In fact, the correlation between the

232   PC1 time series of H200 EOF1 (Fig. 4b) and the PC1 time series of the IWPD (Fig.

233   2b) is 0.88, which is statistically significant at the 99% level. In view of these

234   resemblances to the wave train in the regression map, it is suggested that the wave

235   train triggered by the IWPD represents the dominant mode of the interannual

236   variability of the Asian atmospheric circulation during winter.

237   To further confirm that the teleconnection pattern is a Rossby wave train forced in

238   the tropics, the associated wave-activity flux is shown in Fig. 4c. The wave-activity

239   flux is defined and formulated by Takaya and Nakamura (2001). Consistent with the

240   teleconnection pattern from the IWP to East Asia, the wave-activity flux emits from

241   the tropics towards the Sea of Japan. This indicates that the poleward Rossby wave

242   propagation is related to the teleconnection pattern.

243   In summary, our analyses of observational data show that there is a new

244   atmospheric teleconnection pattern from the IWP to East Asia and the teleconnection

245 pattern may be a Rossby wave train forced by the heating anomalies associated with

246 the IWPD. In next section, we will use a simple atmospheric model to investigate

247 atmospheric responses to various heating distributions.

248

249 *4.2. Results from simple atmospheric model experiments*

250 In this subsection, we use simple atmospheric model experiments to test and

251 confirm the observed results in the last section. According to the spatial pattern of the

252 IWPD, a dipolar heating pattern as observed in the IWP is used to represent the

253 dominant forcing of the winter rainfall anomaly, with a positive heating centered in 0°,

254 60°E and a negative heating centered in 5°N, 125°E. Each center of the heating has a

255 Gaussian-shape:

256

257
$$Q = Q_0 \exp\left[-\left(\frac{\theta - \theta_0}{L_\theta}\right)^2\right] \exp\left[-\left(\frac{\lambda - \lambda_0}{L_\lambda}\right)^2\right], \qquad (1)$$

258

259 where θ is latitude and λ is longitude. The parameter values of Eq. (1) for each

260 experiment are summarized in Table 1. Similar to other simple models, the heating is

261 applied to the level at 500 hPa. The basic mean states are set to the values in winter

262 (DJF). The basic flow is obtained by using the stream functions at 250 hPa and 750

263 hPa from the monthly NCEP-NCAR reanalysis. The stream functions at 750 hPa are

264 constructed by linear interpolation, as 750 hPa is not a standard pressure level. For all

265 cases in the study, the basic flow varies zonally rather than the zonally averaged as in

266 Wang et al. (2010). Since the model atmosphere consists of two levels (centered at

12

267 250 hPa and 750 hPa), the variables can be separated into the barotropic and

268 baroclinic components:

$$\overline{Y} = 0.5(Y_1 + Y_2), \qquad (2)$$
$$\hat{Y} = 0.5(Y_1 - Y_2). \qquad (3)$$

269

270 Here Y stands for any variable with subscripts 1 and 2 denoting values at the upper

271 (250 hPa) and lower (750 hPa) levels, respectively.

272 Figure 5a shows the model response of the barotropic stream function in the case of

273 the dipolar heating forcing of the IWPD. The response shows a pattern of alternating

274 high and low centers from the IWP to East Asia and the northwest Pacific. The wave

275 train of barotropic steam function is similar to that of observations (Figs. 3 and 4). But

276 in the model, the wave train induced by the IWPD heating anomalies can even

277 propagate to North America (Fig. 5a). Two other experiments (Cases 2 and 3) are run

278 with the single polar heat forcing over the WIO and over the EI-WP, respectively. In

279 the case forced by the heating over the WIO, the wave train is very weak (Fig. 5b).

280 But the wave train is strong in the case forced by the cooling over the EI-WP (Fig. 5c),

281 which is comparable with the combined case (Fig. 5a). This indicates that the cooling

282 over the EI-WP is the major contributor to the wave train.

283 The SST anomaly in the tropical eastern Pacific and the corresponding rainfall

284 anomaly in the equatorial central Pacific are closely related to the IWPD. A natural

285 question is whether the heating anomaly in the equatorial central Pacific can make

286 any contribution to the wave train emitted from the IWP to East Asia and the

287 northwest Pacific. The model experiment with single heating in the tropical central or

288 eastern Pacific (EP) is performed (Case 4 in Table 1). In this case, the response of

289 barotropic stream function shows a wave train over the eastern Pacific and North

290 America, which lies east of the location of classical PNA pattern. Note that the wave

291 train is more similar to the classical PNA pattern if the basic mean flow is replaced

292 with the zonally averaged one in the model (not shown). The signal over the

293 IWP-East Asia is very weak (Fig. 5d). This indicates that the heating in the equatorial

294 central Pacific has little direct influence on the wave train from the IWP to East Asia

295 and the northwest Pacific.

296   In brief, the results of the simple model experiments verify and confirm that the

297 IWPD atmospheric heating can induce a wave train from the IWP to East Asia and the

298 northwest Pacific. Either of the isolated anomalous heating or cooling associated with

299 the IWPD can trigger the wave train, but their combination produces the wave train

300 much closer to the observed one.

301   As shown in Lee et al. (2009) and Wang et al. (2010), the background mean zonal

302 winds are important for the propagation of heating-induced signals from the tropics to

303 high latitudes in the Atlantic. The background vertical wind shear is important in

304 converting energy from the heating-induced baroclinic flow anomalies into barotropic

305 motions near the heating source. Then the barotropic flow anomalies in turn interact

306 with the background vertical mean wind to transmit the barotropic signals to the high

307 latitudes. To examine the effect of the background mean flow on the wave train

308 induced by IWPD heating, two model experiments (Cases 5 and 6) are performed

309 with purely barotropic or baroclinic background flows (i.e. $\hat{U}=0, \overline{U}=0$) over the

310 Northern Hemisphere (Fig. 6). The baroclinic responses to IWPD heating in the two

311 experiments are similar (Figs. 6b and d), and resemble those with the realistic

312 background flow experiment (not shown). It is indicated that the baroclinic response

313 to tropical heating is largely independent of the background mean state. But the

314 barotropic stream function response is very different. With no background vertical

315 wind shear (Fig. 6a), the barotropic stream function anomalies are nearly zero in the

316 Northern Hemisphere because the heating-induced baroclinic anomalies cannot

317 interact with the background vertical wind shear to produce barotropic anomalies in

318 the Northern Hemisphere. Besides, with no background vertical mean wind, the

319 barotropic stream function anomalies are too weak to propagate into high latitudes

320 (also see Fig. 6c). Therefore, the model experiments show that the background mean

321 flow is important for the IWPD heating-induced signals to propagate to East Asia and

322 the northwest Pacific.

323

324 *4.3 Decadal change of IWPD and the teleconnection pattern*

325 In the preceding sections, it is shown that a new teleconnection pattern to Asia and

326 the northeast Pacific is induced by the IWPD based on the CMAP rainfall data during

327 1979-2008. Does the teleconnection pattern exist only in this period? In this

328 subsection, we use the PREC data covering from 1948 to 2009 to examine whether

329 the IWPD and the teleconnection pattern display changes across the 1976/77 climate

330 regime shift. For convenience, the period of 1948-1976 and 1977-2009 are called the

331 PRE and POST epoch, respectively.

332 The top two panels of Fig. 7 show the EOF1 and the corresponding PC time series

of DJF precipitation anomalies over the IWP for the PRE (left panels) and POST

(right panels) epoch, respectively. In each period, EOF1 features a dipole pattern with

enhanced rainfall over the Indian Ocean and reduced rainfall over the EI-WP,

resembling the pattern obtained from the CMAP data of the period 1979-2008. By

comparing the patterns in these two epochs, one can see that the IWPD is stronger in

POST than that in PRE, with an additional rainfall anomaly center (<-1.5 mm/day) to

the north of New Guinea in POST (Figs. 7a and b). The IWPD also accounts for a

greater fraction of variance in POST than in PRE (55.6% versus 49.2%). In the

regression maps of H200 anomalies on the time series of the IWPD (Figs. 7e and f),

both the PNA-like pattern and the new teleconnection pattern emitted from the IWP

towards Asia are more obvious in POST than those in PRE, corresponded to the

IWPD strength.

We perform an extra pair of model experiments (Cases 7 and 8) to confirm that the

decadal change of the IWPD is responsible for the teleconnection pattern decadal

change. The difference between these two experiments is that the heating forcing has

stronger amplitude in Case 8 than in Case 7 (Table 1). The model results show that

the barotropic stream function anomalies are stronger over Asia, Sea of Japan and the

northern Pacific in Case 8 (Fig. 8b), indicating a stronger teleconnection pattern with

the stronger heat forcing in the EI-WP region.

As indicated in the last subsection, the background mean flow is important for the

IWPD heating-induced signals to propagate to East Asia and the northwest Pacific.

We also examine whether or not the background mean flow change contributes to the

355 teleconnection pattern decadal change. The result shows that the difference of

356 background mean flows in the PRE epoch and POST epoch is very small, thus has

357 little influence on the decadal change of the teleconnection pattern (not shown). Thus,

358 we can conclude that the decadal change of the teleconnection pattern is mainly due to

359 the intensification of the IWPD after the climate shift of the 1970s.

360

361 **5. Summary and discussion**

362 In this study, the interannual variability of rainfall in the tropical Indo-Western

363 Pacific (IWP) and its influence on Asian and northwest Pacific atmospheric

364 circulation during boreal winter are analyzed. It is found the leading mode of rainfall

365 variability is a dipolar pattern mode, with more rainfall in the tropical western Indian

366 Ocean and less rainfall in the tropical eastern Indian Ocean and Maritime

367 Continent/tropical western Pacific. This pattern is called the tropical Indo-Western

368 Pacific Dipole (IWPD) mode.

369 The analysis of observational data reveals that the convective heating associated

370 with the IWPD pattern can trigger a wave train emitted from the IWP to East Asia and

371 the northwest Pacific, with reduced H200 over Asia (centered at 30°N, 110°E) and

372 enhanced H200 over the northeast part of China/Korean peninsula/Japan (centered at

373 45°N, 140°E). The wave train represents the teleconnected pattern induced by the

374 IWDP heating, influencing the Asian atmospheric circulation in winter. At lower level

375 of the troposphere, associated with this pattern is an anomalous anticyclone east to

376 Japan.

377   A simple model forced by heating anomalies confirms and supports the

378   IWPD-induced teleconnection. The wave train from the IWP to East Asia and the

379   northwest Pacific is triggered by the IWPD heating anomalies. The model

380   experiments also show that the direct effect of heating in the tropical central Pacific

381   (associated with ENSO heating) on the wave train is very small. The model results

382   indicate that the background mean flow is important for the tropical signals to

383   transmit from the IWP to East Asia and the northwest Pacific. Both the IWPD and the

384   wave train display a change across the 1976/77 climate regime shift. Because the

385   IWPD is intensified after the climate shift, the wave train emitted from the IWP to

386   East Asia and the northwest Pacific is stronger during the POST epoch.

387   The SST anomaly pattern associated with the IWPD is the IOD and ENSO SST

388   anomaly distribution (Figs. 3a, c). Although the numerical experiment shows small

389   effect of the heating associated rainfall anomaly in equatorial central Pacific on the

390   wave train in East Asia, the SST anomalies over equatorial eastern Pacific are still

391   important to the western Pacific. Previous studies have shown El Niño could reduce

392   the rainfall and suppress the convection over the western Pacific through the change

393   of the Walker circulation (e.g. Zhang et al. 1996; Wang 2002; Alexander et al. 2004).

394   The observational analyses show that the IWPD and the wave train usually occur in El

395   Niño years (Fig. 2b; Fig. 4b). A natural question is: Can the IOD and/or ENSO lead to

396   the IWPD and then the wave train from the IWP to East Asia and the northwest

397   Pacific? The study by Cai et al. (2011) pointed out that the IOD can trigger a wave

398   train propagating into the extratropics in the Southern Hemisphere during SON.

399   Can/how we predict the IWPD and the wave train based on the preceding SST

400   anomaly in the tropics? Why does the IWPD exhibit a change across the 1976/77

401   climate regime shift? All these issues need be addressed by further studies.

402

403   **Acknowledgments**

411

Reference

Alexander MA, Blade I, Newman M, Lanzante JR, Lau N-C, Scott JD (2002) The Atmospheric Bridge: the Influence of ENSO Teleconnections on Air-Sea Interaction Over the Global Oceans. J Clim 15: 2205-2231.

Alexander M A, Lau N-C, Scott JD (2004) Broadening the atmospheric bridge paradigm: ENSO teleconnections to the North Pacific in summer and to the tropical west Pacific- Indian Oceans over the seasonal cycle. Earth Climate: The Ocean-Atmosphere Interaction. eds. C. Wang, S.-P. Xie and J. Carton. AGU Monograph. pp. 85-104.

Arkin, Smith TM (2003) Reconstruction of the oceanic precipitation from 1948 to the present. the AMS 14th Symposium on Global Change and Climate Variations, Long Beach, CA, 2003.

Cai W, Rensch PV, Cowan T, Hendon HH (2011) Teleconnection Pathways of ENSO and the IOD and the Mechanisms for Impacts on Australian Rainfall. J Clim 24: 3910-3923.

Chen M, Xie P, Janowiak JE, Arkin PA (2002) Global Land Precipitation: A 50-yr Monthly Analysis Based on Gauge Observations. J of Hydrometeorology 3: 249-266.

Fan L, Liu Z, Liu Q (2011) Robust GEFA Assessment of Climate Feedback to SST EOF Modes. Adv. Atmos. Sci., 28(4): 907-912.

Frankignoul C, Czaja A, L'Heveder B (1998) Air-sea feedback in the North Atlantic

434   and surface boundary conditions for ocean models. J. Clim., 11: 2310-2324

435   Gill AE (1980) Some simple solutions for heat-induced tropical circulation. Q J R

436   Meteorol Soc 106: 447–462.

437   Horel JD, Wallace JM (1981) Planetary-scale atmospheric phenomena associated with

438   the Southern Oscillation. Mon Wea Rev 109: 813–829.

439   Hoskins BJ, Karoly DJ (1981) The steady linear response of a spherical atmosphere to

440   thermal and orographic forcing. J Atmos Sci 38: 1179–1196

441   Huang R, Sun F (1992) Impacts of the tropical western Pacific on the East Asian

442   summer monsoon. J Meteorol Soc Jpn 70: 243-256.

443   Kalnay E et al (1996) The NCEP/NCAR 40–Year Reanalysis Project. Bull Am

444   Meteorol Soc 77: 437–471.

445   Klein S A, Sode BJ, Lau N-C (1999) Remote sea surface temperature variations

446   during ENSO: Evidence for a tropical atmospheric bridge. J Clim 12: 917-932.

447   Kosaka Y, Nakamura H (2010) Mechanisms of Meridional Teleconnection Observed

448   between a Summer Monsoon System and a Subtropical Anticyclone. Part I: The

449   Pacific–Japan Pattern. J Clim 23: 5085–5108.

450   Lee S-K, Wang C, Mapes BE (2009) A Simple Atmospheric Model of the Local and

451   Teleconnection Responses to Tropical Heating Anomalies. J Clim 22: 272–284.

452   Liu Q, Wen N, Liu Z (2006) An observational study of the impact of the North Pacific

453   SST   on   the   atmosphere.   Geophys.   Re.   Lett.,   33:   L18611,

454   doi:10:1029/2006GL026082

455   Matsuno T (1966) Quasi-geostrophic motions in the equatorial area. J Meteorol Soc

456 Jpn 44: 25–43.

457 Nitta T (1987) Convective activities in the tropical western Pacific and their impact

458   on the northern hemisphere summer circulation. J Meteorol Soc Jpn 65:

459   373–390.

460 Reason CJC, Allan RJ, Lindesay JA, Ansell TJ (2000) ENSO and climatic signals

461   across the Indian Ocean basin in the global context: Part I. Interannual composite

462   patterns., Int J Climatol, 20: 1285– 1327.

463 Robertson AW, Mechoso CR (2003) Circulation regimes and low-frequency

464   oscillations in the South Pacific sector. Mon Wea Rev 131: 1566–1576.

465 Saji NH, Goswami BN, Vinayachandran PN, Yamagata T (1999) A dipole mode in

466   the tropical Indian Ocean. Nature 401: 360-363.

467 Smith TM, Reynolds RW, Peterson TC, Lawrimore J (2008) Improvements to

468   NOAA's historical merged land–ocean surface temperature analysis

469   (1880–2006).   J Clim 21: 2283–2296.

470 Takaya K, Nakamura H (2001) A formulation of a phase-independent wave-activity

471   flux for stationary and migratory quasigeostrophic eddies on a zonally varying

472   basic flow. J. Atmos. Sci., 58: 608–627

473 Trenberth, KE, Hurrell JW (1994) Decadal atmospheric-ocean variations in the

474   Pacific. Clim Dyn 9: 303-319.

475 Wallace JM, Gutzler DS (1981) Teleconnections in the geopotential height field

476   during the Northern Hemisphere winter. Mon Wea Rev 109: 784–812.

477 Wang C (2002) Atmospheric circulation cells associated with the El Niño-Southern

478 Oscillation. J. Clim 15: 399-419.

479 Wang C, Weisberg RH, Virmani J (1999) Western Pacific interannual variability

480 associated with the El Niño-Southern Oscillation. J. Geophys. Res. 104:

481 5131-5149.

482 Wang C, Lee S-K, Mechoso CR (2010) Inter-hemispheric influence of the Atlantic

483 warm pool on the southeastern Pacific. J Clim 23: 404–418.

484 Xie P, Arkin PA (1996) Analyses of global monthly precipitation using gauge

485 observations, satellites estimates, and numerical model predictions. J Clim 9:

486 840-858.

487 Xie S-P, Du Y, Huang G, Zheng X-T, Tokinaga H, Hu K, Liu Q (2010) Decadal shift

488 in El Niño influences on Indo-western Pacific and East Asian climate in the

489 1970s. J Clim 23: 3352-3368.

490 Yang J, Liu Q, Xie S-P, Liu Z, Wu L (2007) Impact of the Indian Ocean SST basin

491 mode on the Asian summer monsoon. Geophys Res Lett, 34: L02708,

492 doi:10.1029/2006GL028571.

493 Yang J, Liu Q, Liu Z (2010) Linking Observations of the Asian Monsoon to the

494 Indian Ocean SST: Possible Roles of Indian Ocean Basin Mode and Dipole

495 Mode，J Clim , 23: 5889–5902

496 Zhang R, Sumi A, kimoto M (1996) Impact of El Niño on the East Asia Monsoon: A

497 diagnostic study of the '86/87 and '91/92 events. J. Meteor. Soc. Japan, 74:

498 49-62.

499

500

501

502   **Fig. 1** Climatological mean rainfall (contours) and standard deviation of rainfall

503   anomalies (shading) in DJF. The rainfall data is from the CMAP from 1979-2008.

504   Unit is mm/day.

505

506   **Fig. 2** The first EOF mode (a) and the time series (b) of the rainfall anomalies in the

507   Indo-Western Pacific during DJF. The rainfall data is from the CMAP from

508   1979-2008. The spatial patterns are shown as the rainfall anomaly regressions onto

509   the normalized PC time series. The year number in (b) indicates December of year.

510

511   **Fig. 3** Regressions of SST anomalies (shading) and 200 hPa geopotential height

512   (H200; contours) in (a), of sea level pressure (SLP; contours) and sea surface wind

513   (SSW; vectors) in (b) onto PC1 time series in DJF. (c) Regressions of SON SST

514   anomalies (shading) and SSW (vectors) onto PC1 time series in DJF. In (a) and (b),

515   the green contours denote the 90% confidence level for H200 and SLP, respectively.

516   For SST and SSW, only those exceed the 90% confidence level are plotted.

517

518   **Fig. 4** (a) First EOF mode of DJF H200 anomalies and (b) its time series for the

519   period of 1979-2008, (c) the associated wave-activity flux defined by Takaya and

520   Nakamura (2001) for stationary Rossby waves. The spatial patterns are shown as the

521   H200 anomaly regressions onto the normalized PC time series.

522

Fig. 5 Barotropic stream function anomalies (contours at $1 \times 10^6 \text{m}^2\text{s}^{-1}$ intervals; dash

and blue lines are for negative values; solid and red lines are for positive values)

and heating anomalies (dark shading and solid lines represent positive heating

anomalies; light shading and dotted lines represent negative heating anomalies)

in the simple model experiments for basic mean flows in DJF. Shown are the

model experiments of Case 1 (a), Case 2 (b), Case 3 (c) and Case 4 (d). For the

detail of these experiments, see Table 1

Fig. 6 Stream functions (contours at $1 \times 10^6 \text{m}^2\text{s}^{-1}$ intervals; dash and blue lines are for

negative values; solid and red lines are for positive values) of the barotropic (left

panels) and baroclinic (right panels) components from the simple model

experiments. (a) and (b) are from Case 5 without the background vertical wind

shear over the Northern Hemisphere ($\hat{U} = 0$); (c) and (d) are from Case 6

without the background vertical mean wind over the Northern Hemisphere

($\overline{U} = 0$). Dark shading and solid lines represent positive heating anomalies, and

light shading and dotted lines represent negative heating anomalies

Fig. 7 (top) First EOF mode of DJF rainfall anomalies (shown as regressions onto the

corresponding time series), (middle) the corresponding time series and (bottom)

the regression of H200 (contours at intervals of 10m and dash lines for negative

values; shading exceeds the 90% confidence level) on the rainfall EOF time

544   series for the period of (left) 1948-1976 and (right) 1977-2009. The EOF

545   analyses of rainfall are based on PREC data

546

547   **Fig. 8** Barotropic stream function anomalies (contours at $1\times10^6 m^2 s^{-1}$ intervals) for

548   the model experiments of Case 7 (a) and Case 8 (b). Dash and blue lines are for

549   negative values, and solid and red lines are for positive values. Dark shading and solid

550   lines represent positive heating anomalies, and light shading and dotted lines represent

551   negative heating anomalies

552

Table 1 The parameter values of Eq. (1) and background mean flows used in the simple model experiments.

Expt	Heat forcing			Period for calculating background mean flow
	WIO	EI-WP	EP	
Case 1	$Q_0 = 0.4Q_{0EP}$ * $\theta_0 = 0°, \lambda_0 = 60°E$ $L_\theta = 10°, L_\lambda = 15°$	$Q_0 = -0.5Q_{0EP}$ $\theta_0 = 5°N, \lambda_0 = 125°E$ $L_\theta = 10°, L_\lambda = 25°$	None	1979-2008
Case 2	$Q_0 = 0.4Q_{0EP}$ $\theta_0 = 0°, \lambda_0 = 60°E$ $L_\theta = 10°, L_\lambda = 15°$	None	None	1979-2008
Case 3	None	$Q_0 = -0.5Q_{0EP}$ $\theta_0 = 5°N, \lambda_0 = 125°E$ $L_\theta = 10°, L_\lambda = 25°$	None	1979-2008
Case 4	None	None	$Q_0 = Q_{0EP}$ $\theta_0 = 0°, \lambda_0 = 160°W$ $L_\theta = 5°, L_\lambda = 25°$	1979-2008
Case 5	$Q_0 = 0.4Q_{0EP}$ $\theta_0 = 0°, \lambda_0 = 60°E$ $L_\theta = 10°, L_\lambda = 15°$	$Q_0 = -0.5Q_{0EP}$ $\theta_0 = 5°N, \lambda_0 = 125°E$ $L_\theta = 10°, L_\lambda = 25°$	None	1979-2008 $(\hat{U} = 0)$
Case 6	$Q_0 = 0.4Q_{0EP}$ $\theta_0 = 0°, \lambda_0 = 60°E$ $L_\theta = 10°, L_\lambda = 15°$	$Q_0 = -0.5Q_{0EP}$ $\theta_0 = 5°N, \lambda_0 = 125°E$ $L_\theta = 10°, L_\lambda = 25°$	None	1979-2008 $(\overline{U} = 0)$
Case 7	$Q_0 = 0.4Q_{0EP}$ $\theta_0 = 0°, \lambda_0 = 60°E$ $L_\theta = 10°, L_\lambda = 15°$	$Q_0 = -0.5Q_{0EP}$ $\theta_0 = 5°N, \lambda_0 = 125°E$ $L_\theta = 10°, L_\lambda = 25°$	None	1977-2009
Case 8	$Q_0 = 0.5Q_{0EP}$ $\theta_0 = 0°, \lambda_0 = 60°E$ $L_\theta = 10°, L_\lambda = 15°$	$Q_0 = -0.7Q_{0EP}$ $\theta_0 = 5°N, \lambda_0 = 125°E$ $L_\theta = 10°, L_\lambda = 25°$	None	1977-2009

556    $*Q_{0EP} = 2.5 \times 10^{-2} W/kg(2.15K/day)$
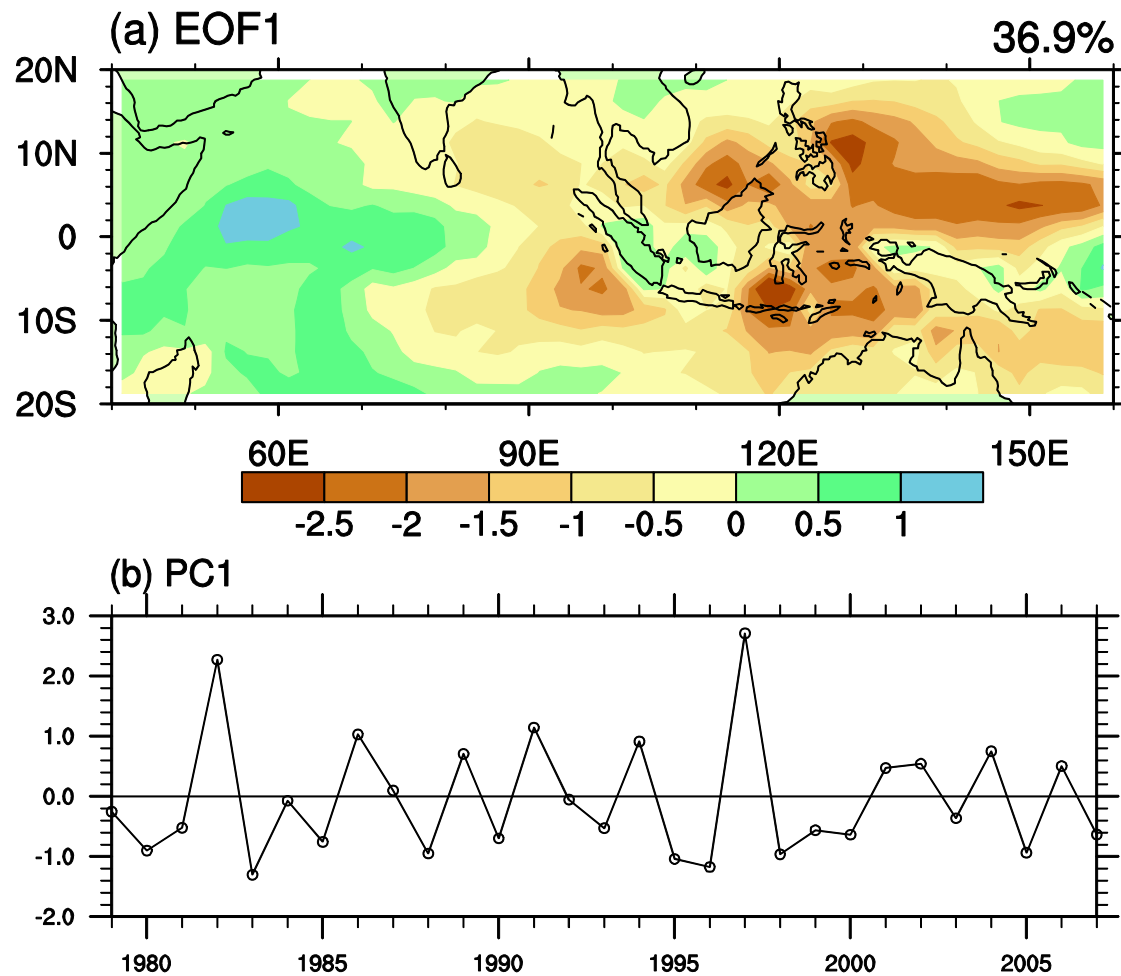
557

DJF Rainfall : Clim. & STD
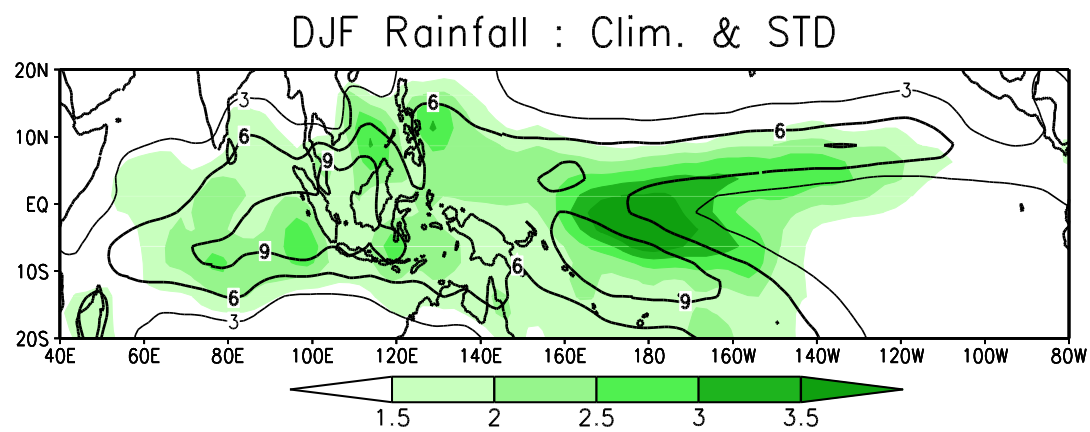
558

559

560 **Fig. 1** Climatological mean rainfall (contours) and standard deviation of rainfall

561 anomalies (shading) in DJF. The rainfall data is from the CMAP from 1979-2008.

562 Unit is mm/day.

563

(a) EOF1   36.9%

(b) PC1

Fig. 2 The first EOF mode (a) and the time series (b) of the rainfall anomalies in the Indo-Western Pacific during DJF. The rainfall data is from the CMAP from 1979-2008. The spatial patterns are shown as the rainfall anomaly regressions onto the normalized PC time series. The year number in (b) indicates December of year.
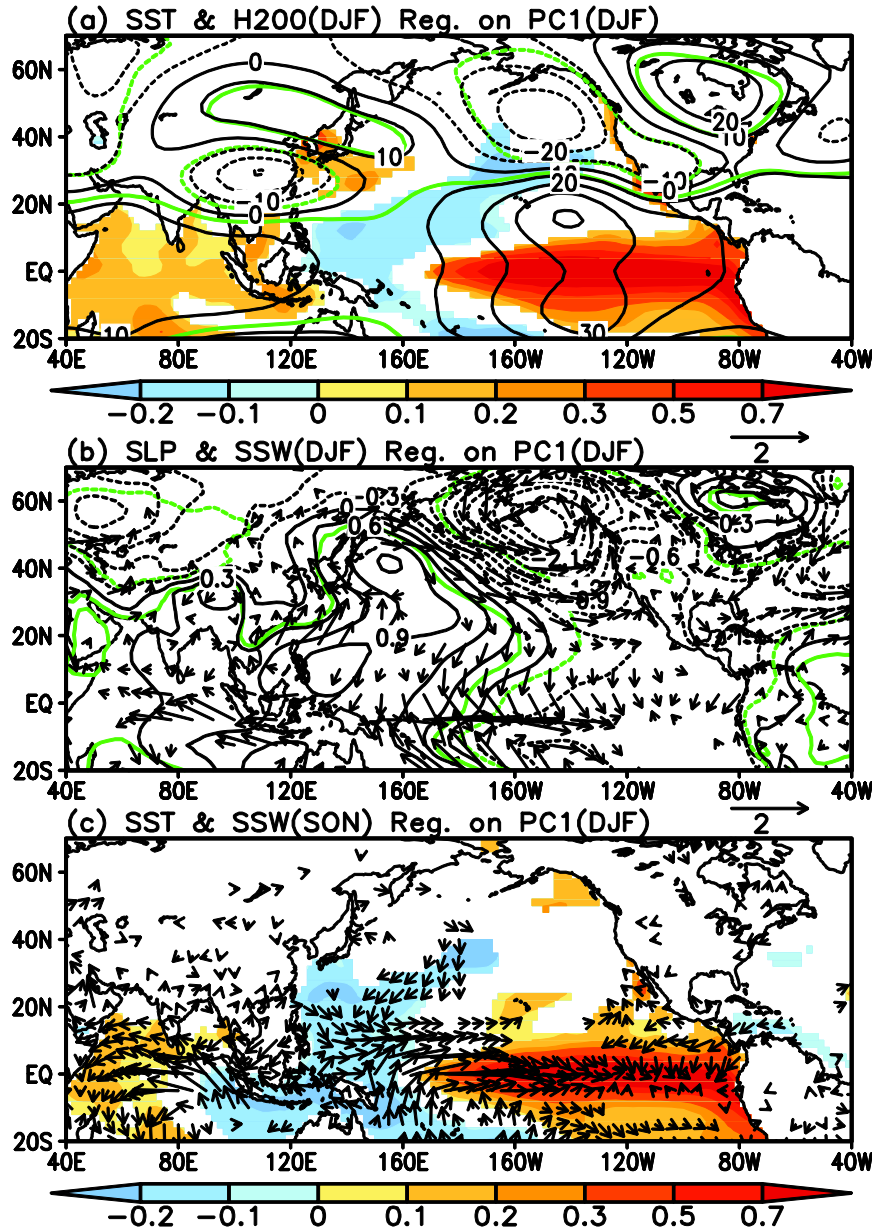
Fig. 3 Regressions of SST anomalies (shading) and 200 hPa geopotential height (H200; contours) in (a), of sea level pressure (SLP; contours) and sea surface wind (SSW; vectors) in (b) onto PC1 time series in DJF. (c) Regressions of SON SST anomalies (shading) and SSW (vectors) onto PC1 time series in DJF. In (a) and (b), the green contours denote the 90% confidence level for H200 and SLP, respectively. For SST and SSW, only those exceed the 90% confidence level are plotted
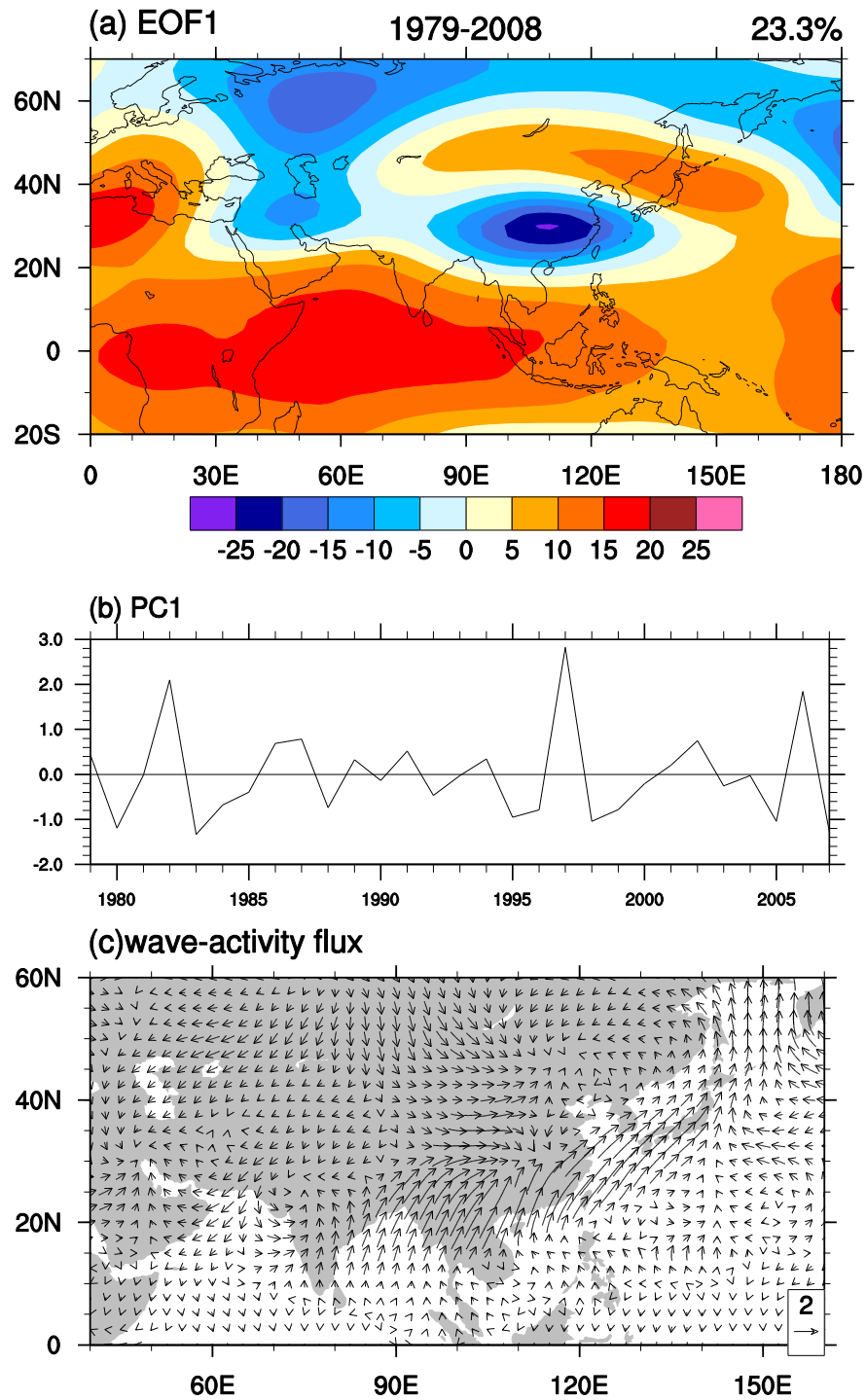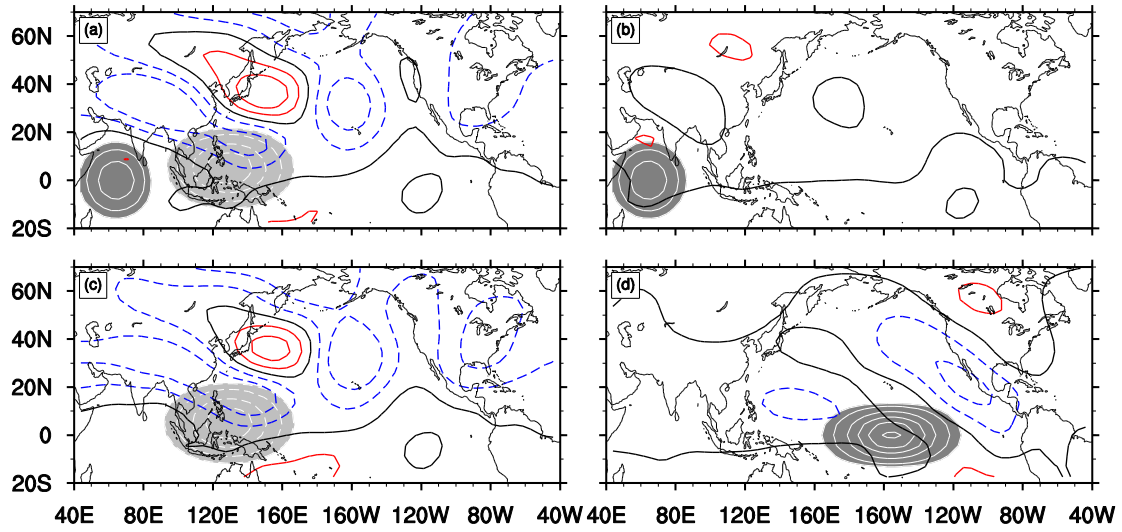
Fig. 4 (a) First EOF mode of DJF H200 anomalies and (b) its time series for the period of 1979-2008, (c) the associated wave-activity flux defined by Takaya and Nakamura (2001) for stationary Rossby waves. The spatial patterns are shown as the H200 anomaly regressions onto the normalized PC time series.

Barotropic Stream Function

Fig. 5 Barotropic stream function anomalies (contours at $1\times10^{6}\mathrm{m}^{2}\mathrm{s}^{-1}$ intervals; dash and blue lines are for negative values; solid and red lines are for positive values) and heating anomalies (dark shading and solid lines represent positive heating anomalies; light shading and dotted lines represent negative heating anomalies) in the simple model experiments for basic mean flows in DJF. Shown are the model experiments of Case 1 (a), Case 2 (b), Case 3 (c) and Case 4 (d). For the detail of these experiments, see Table 1
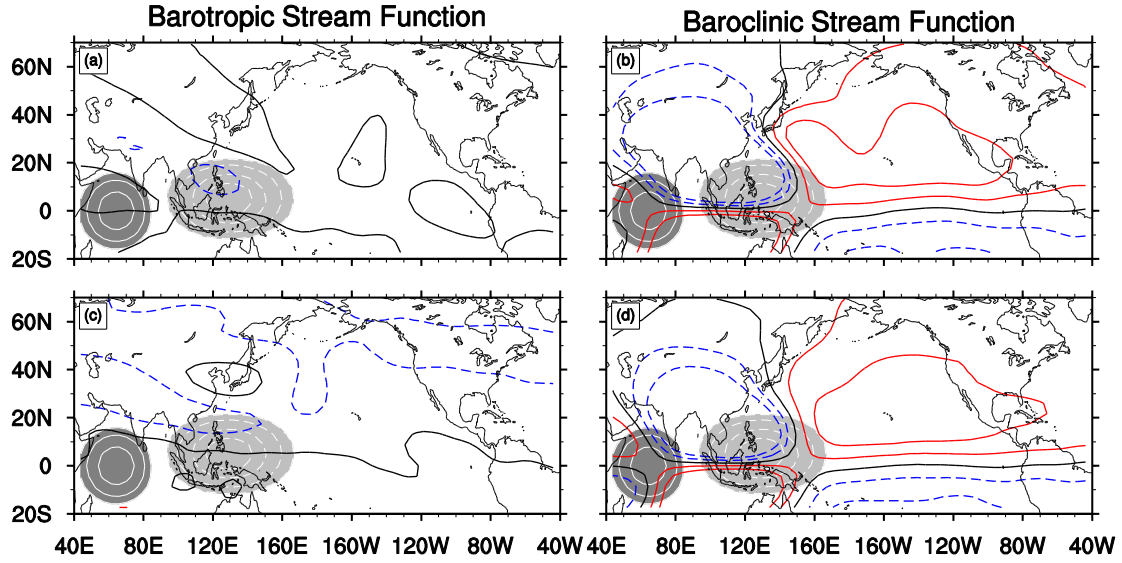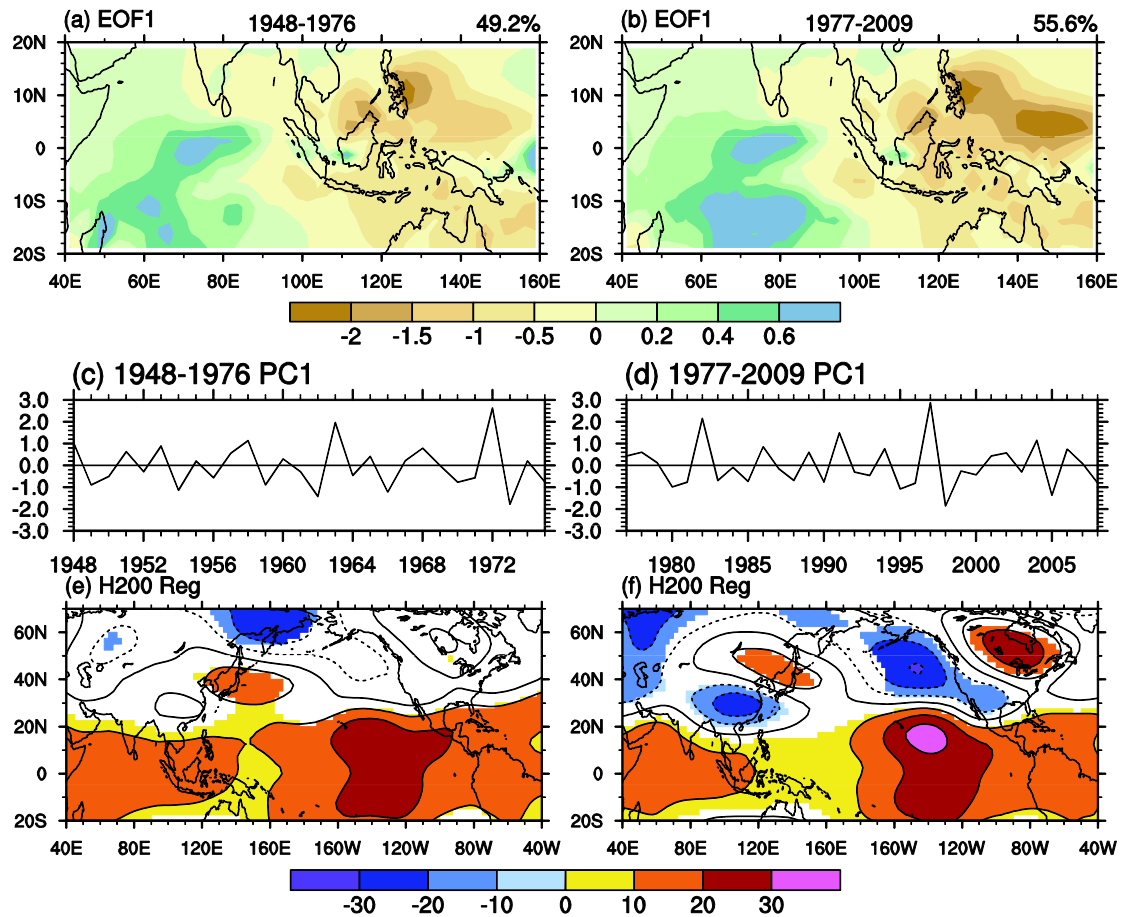
Fig. 6 Stream functions (contours at $1 \times 10^6 \mathrm{m}^2\mathrm{s}^{-1}$ intervals; dash and blue lines are for negative values; solid and red lines are for positive values) of the barotropic (left panels) and baroclinic (right panels) components from the simple model experiments. (a) and (b) are from Case 5 without the background vertical wind shear over the Northern Hemisphere ($\hat{U} = 0$); (c) and (d) are from Case 6 without the background vertical mean wind over the Northern Hemisphere ($\overline{U} = 0$). Dark shading and solid lines represent positive heating anomalies, and light shading and dotted lines represent negative heating anomalies
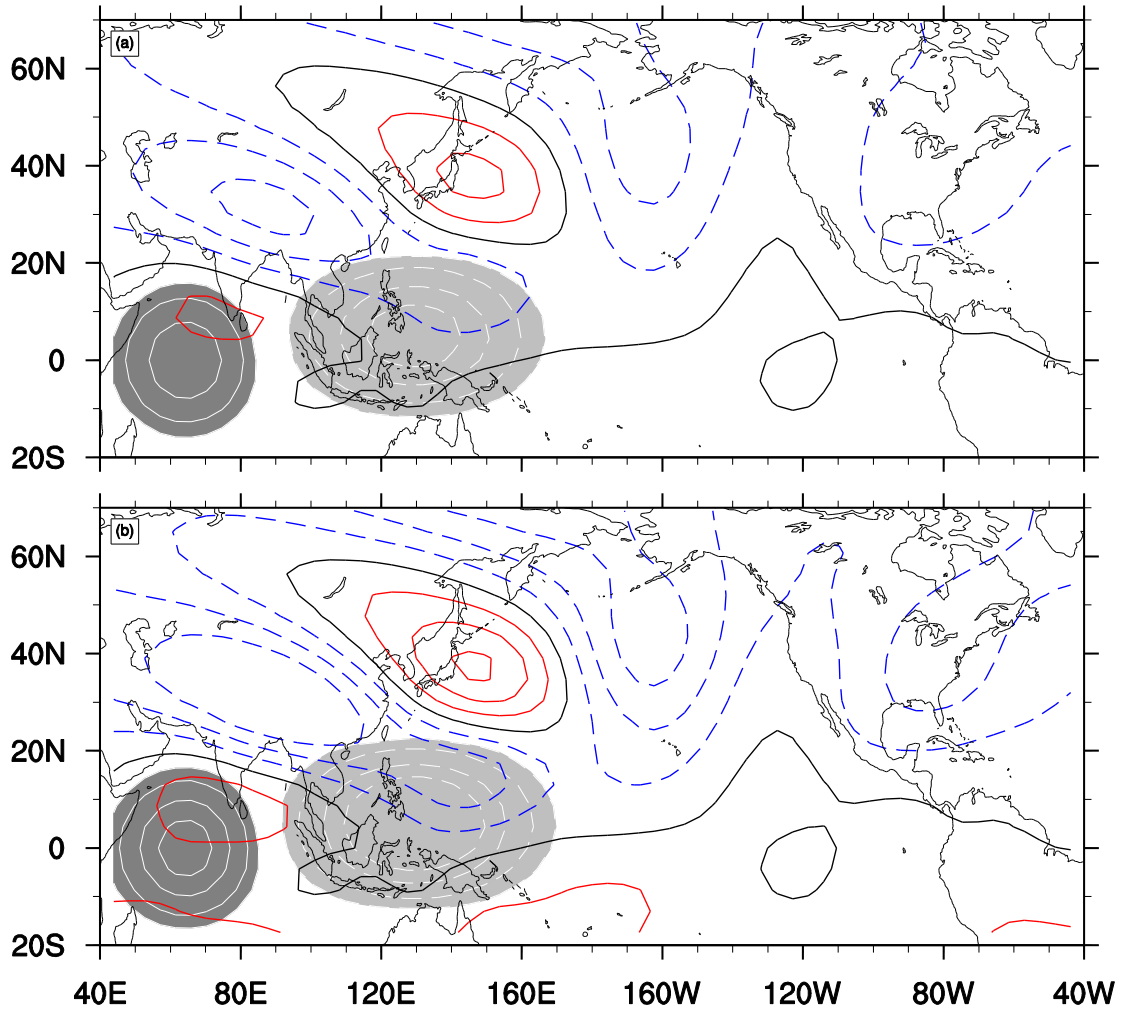
Fig. 7 (top) First EOF mode of DJF rainfall anomalies (shown as regressions onto the corresponding time series), (middle) the corresponding time series and (bottom) the regression of H200 (contours at intervals of 10m and dash lines for negative values; shading exceeds the 90% confidence level) on the rainfall EOF time series for the period of (left) 1948-1976 and (right) 1977-2009. The EOF analyses of rainfall are based on PREC data.

Barotropic Stream Function

617

Fig. 8 Barotropic stream function anomalies (contours at $1 \times 10^{6} m^{2} s^{-1}$ intervals) for the

model experiments of Case 7 (a) and Case 8 (b). Dash and blue lines are for negative

values, and solid and red lines are for positive values. Dark shading and solid lines

represent positive heating anomalies, and light shading and dotted lines represent

negative heating anomalies